Coarse-Graining the Fluid Flow around a Human Sperm

Kenta Ishimoto,[1,2] Hermes Gadêlha,[3,6,7] Eamonn A. Gaffney,[4] David J. Smith,[5,6,7] and Jackson Kirkman-Brown[6,7]
[1]*The Hakubi Center for Advanced Research, Kyoto University, Kyoto 606-8501, Japan*
[2]*Research Institute for Mathematical Sciences, Kyoto University, Kyoto 606-8502, Japan*
[3]*Department of Mathematics, University of York, York YO10 5DD, United Kingdom*
[4]*Wolfson Centre for Mathematical Biology, Mathematical Institute, University of Oxford, Oxford OX2 6GG, United Kingdom*
[5]*School of Mathematics, University of Birmingham, Birmingham B15 2TT, United Kingdom*
[6]*Institute for Metabolism and Systems Research, College of Medical and Dental Sciences,*
University of Birmingham, Birmingham B15 2TT, United Kingdom
[7]*Centre for Human Reproductive Science, Birmingham Women's NHS Foundation Trust,*
Birmingham B15 2TG, United Kingdom

(Received 5 December 2016; published 23 March 2017)

The flagellar beat is extracted from human sperm digital imaging microscopy and used to determine the flow around the cell and its trajectory, via boundary element simulation. Comparison of the predicted cell trajectory with observation demonstrates that simulation can predict fine-scale sperm dynamics at the qualitative level. The flow field is also observed to reduce to a time-dependent summation of regularized Stokes flow singularities, approximated at leading order by a blinking force triplet. Such regularized singularity decompositions may be used to upscale cell level detail into population models of human sperm motility.

DOI: 10.1103/PhysRevLett.118.124501

Introduction.—The flagellum is a moving whiplike cellular appendage found on numerous protozoa and the spermatozoa of almost all species. In particular, the subject of male subfertility has led to extensive quantitative studies of human sperm motility [1–4], while even single cell studies can generate extensive information, in particular, from digital imaging microscopy. However, the tools for examining human sperm digital imaging microscopy are founded from an era where only the cell body, and not the flagellum, could be readily resolved [1,2]. Apart from some simulations of velocity magnitude [5] and surface attraction [6], there is relatively less detailed characterization of the fluid dynamics associated with the human sperm flagellar beat.

More extensive characterization of the fluid dynamics of other flagellates is available. For instance, flows have been reconstructed from the flagellar waveform for the algae *C. reinhardtii*, using numerical simulation [7,8], though validation of simulations to actual swimmer dynamics has been limited to the approximation of resistive force theory [9] and required resistance coefficients that varied extensively between different sperm. Furthermore, flows around microswimmers have been measured using micro-particle image velocimetry for Gardia protozoan flagellates [10], though reported with limited resolution. Analogous studies have been pursued for *C. reinhardtii*, though reported with an averaging, either temporal or spatial, [11,12] or in a single plane [12,13]. Such simplifications in the reported data particularly emphasize the need to simplify the velocity flow fields, even in focused studies.

Principal component analysis (PCA) has been used to reduce the dimensionality of flagellar data [14,15], though such approaches have not been applied to the associated flow fields generated by the flagellum beat, despite the complexity of these data sets. Instead, a small number of viscous flow singularities have been used to approximate time-averaged microswimmer flows (e.g., [11]) and are popular since singularity flows have a clear theoretical interpretation as the first terms of a multipole expansion. However, temporal averaging may be ill advised [8], since the time dependence of microswimmer flows persists on length scales associated with cell-cell hydrodynamic interaction, increasing the complexity of information that needs to be retained.

Thus, the primary objective of this Letter is to demonstrate that it is possible to systematically reduce the flow field associated with a swimming human sperm in terms of a time-dependent superposition of regularized viscous flow singularities, via an intermediate PCA analysis of the flow field. In turn, this has prospective use as a framework for facilitating theoretical interpretation and investigation. In the intermediate steps of these procedures, we digitize the flagellar waveform and use boundary element simulation to determine the fluid flow surrounding the sperm, which will also generate predictions for the cell trajectory. Thus, *en route* to the singularity representation of the flow field, we will also have the objective of comparing predictions for the human sperm trajectory with observation, to assess both the use of digitized flagellar waveforms and numerical simulation for predicting fine-scale human sperm motility at the qualitative level. Once the singularity representation of the flow field has been obtained, our final objective will be to analyze the representation in terms of concepts from dynamical systems theory to consider potential insights concerning the dynamics of human sperm swimming and the flows it induces.

Imaging.—The experimental methodology is further detailed in Smith *et al.* [3]. In summary, human sperm samples were collected from a normozoospermic research donor; sperm that had penetrated approximately 2 cm into a capillary tube containing a saline medium were imaged in the region of cell accumulation approximately 10–20 μm from the capillary tube inside surface (Supplemental Material, Movie 1 [16]). The imaging was conducted with an Olympus (BX-50) microscope with halogen illumination and a positive phase contrast lens ($20\times/0.40\,\infty/0.17$ Ph1 together with a depth of field of approximately 5.8 μm) and a Hamamatsu Photonics K.K. C9300 CCD camera at 292 frames per second, streaming data directly to a Dell Dimension workstation, running Wasabi software (Hamamatsu Photonics).

A time sequence of flagellar position data in the microscope focal plane was extracted from the imaging data, using custom MATLAB© software [3]. This analysis provided the angle $\psi(s,t)$, between the local tangent of the flagellum and the sperm head, with s denoting the arclength along the flagellum from the proximal to the distal end, and with t denoting time. The extracted flagellar waveform contains more than six flagellar periods [Figs. 1(a) and 1(b)], with a primary beat and a series of smaller undulations in the proximal region possessing an approximately threefold higher frequency, as reported in Smith *et al.* [3].

Reconstruction of the flagellar waveform.—Following the shape analysis of bull spermatozoa by Ma *et al.* [14], as reviewed in Ref. [15], we implemented PCA for the angle ψ to determine a flagellar shape decomposition. In particular, with the arclength discretized into m values, $s_1,\ldots,s_m$, and time discretized into n values, $t_1,\ldots,t_n$, we have the angle matrix $\psi_{i\alpha}=\psi(t_i,s_\alpha)$, and its temporal average $\bar{\psi}_{i\alpha}=(1/n)\sum_{p=1}^{n}\psi_{p\alpha}$ for any $i\in\{1,\ldots,n\}$.

The eigenvectors of the $m\times m$ covariance matrix, $S_{\alpha\beta}=(1/n)\sum_{i=1}^{n}(\psi_{i\alpha}-\bar{\psi}_{i\alpha})(\psi_{i\beta}-\bar{\psi}_{i\beta})$, provide a basis for the flagellar wave, with m eigenvectors, $\{\mathbf{a}_1,\ldots,\mathbf{a}_m\}$, ordered by the size of the associated eigenvalues $\lambda_1\geq,\ldots,\geq\lambda_m$. Each eigenvector corresponds to a set of angles that define a flagellum shape, and the first three eigenvectors, also known as PCA modes and associated with eigenvalues $\lambda_1,\ldots,\lambda_3$, are plotted in Fig. 1(c). In particular, the first two PCA modes capture 95.9% of the cumulative variance, that is $(\lambda_1+\lambda_2)/\mathrm{trace}(S)=0.959$, while the first three capture 99.3%. Thus, respectively, there is a 4.1% and 0.7% variation in the flagellar shape that is not accounted for in projecting the flagellar data for all arclength and time onto the span of these PCA modes, demonstrating data reduction with limited sacrifice in accuracy.

The time-dependent coefficients when expressing the flagellar angle as a summation of PCA modes also define trajectories in the PCA phase shape space; for the expansion in the first two modes, this yields dumbbell-like trajectories, as plotted in Fig. 1(d). By mapping the time-dependent trajectory in the phase space with a phase parameter [14,19], a phase space limit cycle can be determined, as given by the red curve in Fig. 1(d), and will be used below to provide a characteristic waveform for the human sperm.

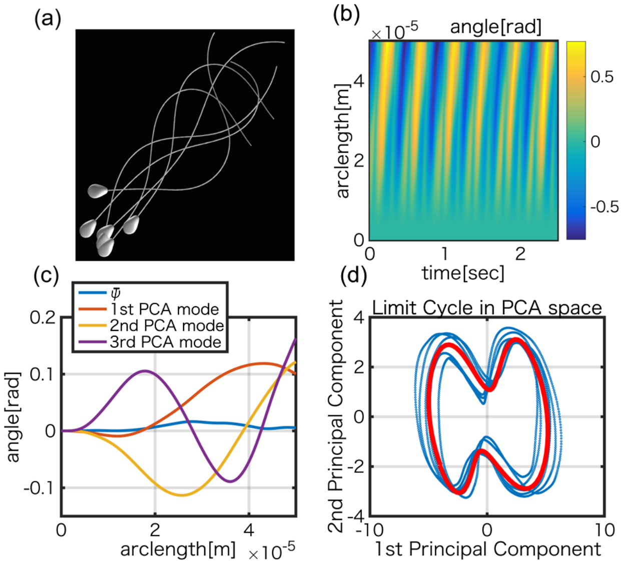

FIG. 1. Sperm flagellar waveform and its reconstruction. (a) Flagellar reconstruction using three PCA modes. (b) Flagellar tangent angle, $\psi(s,t)$. Note that approximately 10% of the distal flagellum data are lost during image capture. (c) The first three PCA modes of the flagellum angle, ψ, where $\bar{\psi}$ is the temporal average of the angle. (d) The trajectory of the first two PCA mode coefficients (blue), with the associated limit cycle orbit, in the phase space (red).

Boundary elements and the swimming trajectory.—The fluid flow field around the sperm and its predicted trajectory were determined via boundary element methods (BEM) [20] (Supplemental Material, Movie 2 [16]). The computational human spermatozoon has a prolate ellipsoid head connected to a cylindrical flagellum, as shown in Fig. 1(a). The waveform is reconstructed using the three-dimensional phase space limit cycle in Fig 1(d).

Before considering the velocity vector field, we compare the predicted and observed sperm trajectory. Surprisingly, despite the fact that the two-dimensional PCA mode expansion loses only 4.1% of the waveform variance, the resulting swimming trajectory fails to capture characteristics of sperm yawing, as displayed in Fig 2. When the limit cycle associated with the first three PCA modes is used for the waveform, the predicted swimming trajectory compares substantially better with observation, although the overall progressive speed is generally lower (Fig. 2), emphasizing a sensitivity of the hydrodynamics to small changes in the flagella beat pattern. Including the presence

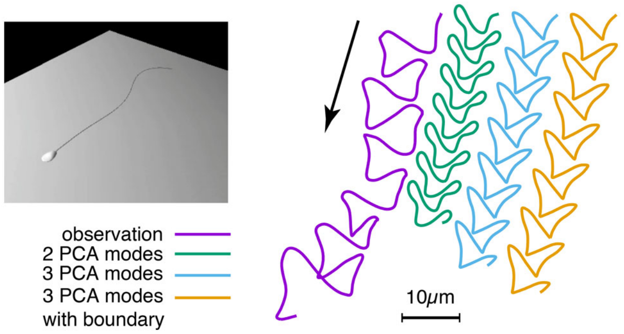

FIG. 2. Observed and predicted sperm head trajectories for different PCA mode truncation. The overall swimming direction is indicated by the arrow. Upper left inset shows the BEM virtual sperm swimming near a solid boundary (Supplemental Material, Movie 2 [16]).

of a nearby wall also marginally increases the numerical swimming speed, highlighting the hydrodynamic influence of nearby no-slip boundaries. The system is also prone to other sources of error: the precise height of the sperm from the cover-slip is not available while, in addition, small 3D flagellar movement inducing nonplanar motions near the distal flagellar tip are not captured. Despite these empirical uncertainties, the overall qualitative agreement between the BEM calculation and observation demonstrates that both simplified three-mode PCA approximation and numerical simulation can be used for understanding and predicting fine-scale sperm motility at the qualitative level.

Velocity field around a spermatozoon.—For simplicity, the BEM calculations for the fluid velocity field relative to the sperm head-tail junction are considered with no external boundaries and are presented in Fig 3 and the Supplemental Material, Movie 3 [16]. The time-averaged velocity field in the near and far field of the flagellar beat plane (xy plane), and in a plane perpendicular to the beat plane ($x = 0$ plane) is shown in Fig. 3 with its magnitude decaying like r^{-2} in the far field [Fig. 3(a)], with r the distance from the head neck junction. This is expected since the swimmer is force free, and thus, the leading term in a multipole expansion of the flow field is $\lambda \mathbf{G}^d$, where $\mathbf{G}^d$ is a Stokeslet dipole. The sign of λ classifies the swimmer as a pusher ($\lambda > 0$) or, conversely, a puller, and fluid moving away from the cell along its long axis in Fig. 3 demonstrates that $\lambda > 0$; hence, unsurprisingly, the time-averaged swimming of the sperm corresponds to a pusher [6].

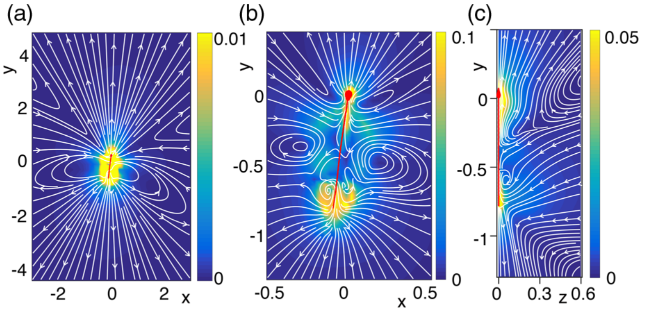

FIG. 3. The time-averaged fluid flow around a human sperm. The flagellum length is $L = 50\ \mu\mathrm{m}$ and the beat period is $T \approx 0.42$ sec. The velocity magnitude is given in units of L/T. (a) The time-averaged far-field flow in the beating plane (xy plane). (b) The time-averaged near-field flow. (c) The time-averaged near-filed flow in $x = 0$ plane, perpendicular to the beating plane. Streamlines are also depicted in white.

Singular decomposition of the flow.—Before attempting to summarize the spatial-temporal fluid velocity field from the BEM calculation in terms of Stokes-flow singularities, PCA is used to reduce complexity. Once more, we have n time values, $t_1, \ldots, t_n$, and with m the number of mesh points in a spatial discretization, let $\alpha \in \{1, \ldots, 3m\}$ index the set $(\mathbf{e}_{q_1(\alpha)}, \mathbf{x}_{q2(\alpha)})$ where, respectively, $q_1(\alpha) \in \{1, 2, 3\}$ is the axis associated with α, and $q_2(\alpha) \in \{1, \ldots, m\}$ is the mesh point associated with α. Then, with $u_{i\alpha} = \mathbf{e}_{q_1(\alpha)} \cdot \mathbf{u}(t_i, \mathbf{x}_{q_2(\alpha)})$, and the velocity field temporal average $\bar{u}_{i\alpha} = (1/n) \sum_{p=1}^{n} u_{p\alpha}$ for any $i \in \{1, \ldots, n\}$, PCA can be implemented for the $3m \times 3m$ covariance matrix $S^{\mathrm{vel}}_{\alpha\beta} = (1/n) \sum_{i=1}^{n} (u_{i\alpha} - \bar{u}_{i\alpha})(u_{i\beta} - \bar{u}_{i\beta})$.

In Fig. 4(a), the first five PCA modes are depicted, and the cumulative variance is close to one for the first five terms of a PCA mode expansion, as shown in Fig. 4(b). While Klindt and Friedrich [8] suggest using unsteady Stokes singularities in multipole expansions, we approximate the steady PCA modes with Stokeslets, though these are regularized [21] in order to avoid actual singularities. Hence, for the velocity field of PCA mode s, we consider $\tilde{\boldsymbol{u}}^s(\boldsymbol{x}) = \sum_{k=1}^{K} \boldsymbol{f}^{(s,k)} \cdot \boldsymbol{G}_{\epsilon^{(s,k)}}(\boldsymbol{x}, \boldsymbol{x}_0^{(s,k)})$, where $\boldsymbol{G}_\epsilon = [(r^2 + 2\epsilon^2)\boldsymbol{I} + \boldsymbol{r}\boldsymbol{r}]/(r^2 + \epsilon^2)^{3/2}$ is the regularized Stokeslet [21], with $\boldsymbol{r} = \boldsymbol{x} - \boldsymbol{x}_0^{(s,k)}$, $r = |\boldsymbol{r}|$, and $\boldsymbol{I}$ denoting the identity tensor. The position of each singularity $\boldsymbol{x}^{(s,k)}$, the associated magnitude $\boldsymbol{f}^{(s,k)}$ and regularization parameter $\epsilon^{(s,k)}$ are calculated via least-square fitting. We use the minimal number of singularities that provide a reasonable fit for each flow PCA mode, in this case $K = 3, 3, 4, 6, 5$ for the lowest five modes. The coefficients for the Stokeslet decomposition are provided in the Supplemental Material [16].

For each time point $i \in \{1, \ldots, n\}$, projecting the $3m$ dimensional vector $u_{i\alpha}$ of the original velocity field onto the span of the velocity vectors $\tilde{u}^s_\alpha = \mathbf{e}_{q_1(\alpha)} \cdot \tilde{\mathbf{u}}^s(\mathbf{x}_{q_2(\alpha)})$, $s \in \{1, \ldots, K\}$ generates an approximation of the velocity field. With $u^{K*}_{i\alpha}$ denoting the projected $3m$ dimensional vector at time point i, one can generate a covariance matrix, $S^{*K}_{\alpha\beta} = (1/n) \sum_{i=1}^{n} (u^{*K}_{i\alpha} - \bar{u}^{*K}_{i\alpha})(u^{*K}_{i\beta} - \bar{u}^{*K}_{i\beta})$, with the temporal average $\bar{u}^{*K}_{i\alpha}$ defined analogously to the average of the observed velocity field. Then, $\mathrm{trace}(S^{*K})/\mathrm{trace}(S^{\mathrm{vel}})$ gives the proportion of the variance in the original flow captured by the K-level regularized Stokeslet approximation, as plotted in the inset of Fig. 4(b). Furthermore, the lowest

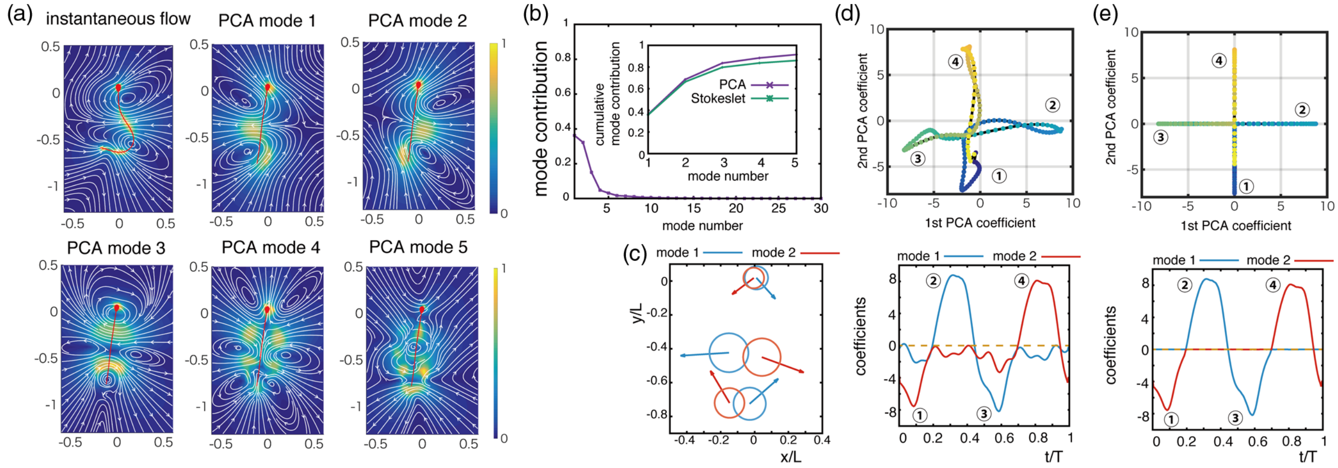

FIG. 4. (a) The first five PCA modes of the time-dependent fluid velocity field, with same units used in Fig. 3. (b) The associated contribution rate of the PCA modes of the velocity field. The inset depicts the cumulative variance of the PCA modes and the regularized Stokeslet approximations. (c) Force triplet approximation for the first two PCA modes of the velocity field. The size and direction of the arrows give the location, magnitude, and direction of the force singularities. The circle radius corresponds to the regularization parameter, ϵ. (d) Top. The upper plot shows the phase space of the first two PCA modes of the velocity field, with color changing with increasing time (blue to yellow). The numbers 1–4 match the labels of (d) lower figure, which shows the time-evolution of the coefficients derived from the regularized force triplet approximation, nondimensionalized by the beat period T. (e) The associated dynamical system approximation of the blinking force triplet, as presented in (d).

two flow PCA modes are each well approximated by a regularized force triplet, with no net force and consisting of one lateral force, together with a force at the sperm head and one near the distal flagellar tip, as summarized in Fig. 4(c). In particular, the force triplet 1 is associated with flow PCA mode 1, whereas force triplet 2 is associated with flow PCA mode 2 in Fig. 4(a).

The time-dependent coefficients of two triplet bases are shown in Fig. 4(d). One can observe, from Fig. 4(b), that these modes capture about 68% of the cumulative variance to provide an overall view of the flow field and, similarly, for the corresponding force triplet, even if finer details are not represented. This figure is augmented to 90% if five modes are considered, instead [inset in Fig. 4(b)]. At point 1 in the phase plane in Fig. 4(d), which also corresponds to $t/T \approx 0$ in the time evolution in Fig. 4(d) lower figure, the flow is essentially that of PCA mode 2, or the equivalent force triplet, with a negative coefficient. Hence, the fluid is moving away from the sperm along its long axis, and thus, the sperm is a pusher at this point. *En-route* to point 2 in the PCA phase portrait in Fig. 4(d), the flow evolves to one with essentially no contribution from force triplet 2 and with the coefficient of force triplet 1 becoming increasingly positive. Hence, at point 2, the fluid is moving from the sperm along its long axis and the sperm is now a puller. On transitioning to point 3 in the phase plane, the flow field reverses, so that force triplet 1 acquires a negative coefficient, and the sperm is a pusher once more. These changes in the coefficients of the force triplets during this evolution along the phase plane orbit are given in Fig 4(d), bottom plot, with the further changes in the coefficients also depicted as the beat cycle passes through point 4, where the sperm is a puller, and then back to point 1, to complete the orbit. The regularized Stokeslet parameters and time-dependent coefficients for the lowest five PCA modes of the velocity field are available in the Supplemental Material, Fig. 1 [16].

With this breakdown of the beat cycle from the systematic reduction of the flow field, one has that the sperm continually switches between pusher and puller modalities, as previously observed for *C. reinhardtii* [8]. In addition, the crosslike structure of the PCA phase portrait orbit in Fig. 4(d) emphasizes that one of the PCA modes, or its associated force triplet, is always essentially off, as also highlighted in Fig. 4(e). This structure and temporal dependence is directly analogous to that of the blinking Stokeslet [22], and with the coefficient approximation indicated in Fig. 4(e), the leading order flow is that of a blinking regularized force triplet. In addition, we note that the systematic reduction not only reveals the blinking as an emergent feature, but also automatically determines how improved accuracy can be achieved via additional regularized singularities.

Finally, while we observed, in Fig. 2, that boundary effects only perturb the predicted trajectory and, hence, our simplification of neglecting external boundaries for the above velocity field study, it is, nonetheless, recognized that the fluid flow close to a no-slip boundary is nontrivially modified [23]. Hence, we have also considered BEM simulations for the case of a spermatozoa swimming parallel to a wall with a height of $z = 0.3\ L \sim 15\ \mu$m. The resulting flow field can still be decomposed into a small number of PCA modes and regularized singularity approximations that capture essentially as much of the variance as the results with no external boundaries, as can be observed by comparing Fig. 2 and Fig. 4(b) in the Supplemental Material [16]. Thus, the use of PCA modes and singularity expansions to summarize, and further explore, the flow field induced by a sperm also retains accuracy in the vicinity of a no-slip boundary despite the added hydrodynamic complexity.

Summary and conclusions.—We have digitized a swimming human sperm beat pattern using its associated limit cycle in a phase space of PCA modes to determine the flow field round the sperm via boundary element numerical simulations. We have also shown that the fluid flow surrounding the cell can be systematically decomposed into a small number of regularized Stokeslets with time dependent coefficients, and the core features of the flow field can be approximated by a blinking regularized force triplet. This decomposition also highlights that, while the sperm head is, on average, pushed by its flagellum, it is also periodically pulled backwards and sideways, as reflected in the observed and predicted swimming trajectories. The general qualitative agreement between observed and predicted trajectories also demonstrates that both simulation and the digitized waveforms can be used for making theoretical predictions about fine-scale human sperm swimming. Finally, we note that the ability to use a small number of regularized singularities to summarize the flow field, including complexities such as the presence of a no-slip boundary, provides a methodology for coarse graining the time-dependent flow around a human sperm for use in developing population level models that retain individual cell dynamics.

Data accessibility.—All data created during this research are openly available by following the link in Ref. [24].

K. I. acknowledges support from the Kyoto University Hakubi Project and the Supporting Program for Interaction-based Initiative Team Studies (SPIRITS). D. J. S. and J. K. B. acknowledge MRC Special Training Fellowship No. G0600178. The authors acknowledge the major contribution of the late Professor John Blake in fostering the research collaboration which led to this work.

[1] S. Mortimer and M. Swan, Hum. Reprod. **10**, 873 (1995).
[2] S. Mortimer, D. Schëväert, M. Swan, and D. Mortimer, Hum. Reprod. **12**, 1006 (1997).
[3] D. Smith, E. Gaffney, H. Gadêlha, N. Kapur, and J. Kirkman-Brown, Cell Motil. Cytoskeleton **66**, 220 (2009).
[4] E. Ooi, D. Smith, H. Gadêlha, E. Gaffney, and J. Kirkman-Brown, J. Roy. Soc. Open Sci. **1**, 140230 (2014).
[5] E. Gaffney, H. Gadêlha, D. Smith, J. Blake, and J. Kirkman-Brown, Annu. Rev. Fluid Mech. **43**, 501 (2011).
[6] D. J. Smith and J. R. Blake, Math. Sci. **34**, 74 (2009).
[7] S. O'Malley and M. Bees, Bull. Math. Biol. **74**, 232 (2012).
[8] G. Klindt and B. Friedrich, Phys. Rev. E **92**, 063019 (2015).
[9] B. Friedrich, I. Riedel-Kruse, J. Howard, and F. Julicher, J. Exp. Biol. **213**, 1226 (2010).
[10] S. Lenaghan, C. Davis, W. Henson, Z. Zhang, and M. Zhang, Proc. Natl. Acad. Sci. U.S.A. **108**, E550 (2011).
[11] K. Drescher, R. Goldstein, N. Michel, M. Polin, and I. Tuval, Phys. Rev. Lett. **105**, 168101 (2010).
[12] G. S. Klindt, C. Ruloff, C. Wagner, and B. M. Friedrich, Phys. Rev. Lett. **117**, 258101 (2016).
[13] J. Guasto, K. Johnson, and J. Gollub, Phys. Fluids **23**, 091112 (2011).
[14] R. Ma, G. Klindt, I. Riedel-Kruse, F. Jülicher, and B. Friedrich, Phys. Rev. Lett. **113**, 048101 (2014).
[15] S. Werner, J. C. Rink, I. H. Riedel-Kruse, and B. M. Friedrich, PLoS One **9**, e113083 (2014).
[16] See Supplemental Material http://link.aps.org/supplemental/10.1103/PhysRevLett.118.124501 for regularized singularity decomposition coefficients and movies associated with this Letter, which includes Refs. [17,18].
[17] J. Ainley, S. Durkin, R. Embid, P. Boindala, and R. Cortez, J. Comput. Phys. **227**, 4600 (2008).
[18] D. J. Smith, Proc. R. Soc. A **465**, 3605 (2009).
[19] B. Kralemann, L. Cimponeriu, M. Rosenblum, A. Pikovsky, and R. Mrowka, Phys. Rev. E **77**, 066205 (2008).
[20] K. Ishimoto and E. A. Gaffney, J. Theor. Biol. **360**, 187 (2014).
[21] R. Cortez, SIAM J. Sci. Comput. **23**, 1204 (2001).
[22] J. Blake and S. Otto, Theor. Comput. Fluid Dyn. **10**, 23 (1998).
[23] D. J. Smith, E. A. Gaffney, J. R. Blake, and J. C. Kirkman-Brown, J. Fluid Mech. **621**, 289 (2009).
[24] University of Oxford Archive: https://doi.org/10.5287/bodleian:1Zvzab18P.